Science Advances AAAS

Manuscript Template

Title

Seasonal slow slip in landslides as a window into the frictional rheology of creeping shear zones

Authors

Noah J. Finnegan[1]*, Demian M. Saffer[2,3]

Affiliations

[1]Department of Earth and Planetary Sciences, University of California, Santa Cruz; Santa Cruz, CA, USA.

[2]Institute for Geophysics, Jackson School of Geosciences, University of Texas at Austin, Austin, TX, USA.

[3]Department of Earth and Planetary Sciences, Jackson School of Geosciences, University of Texas at Austin, Austin, TX, USA.

*Corresponding author. Email: nfinnega@ucsc.edu

Abstract

Whether Earth materials exhibit frictional creep or catastrophic failure is a crucial but unresolved problem in predicting landslide and earthquake hazards. Here we show that field-scale observations of sliding velocity and pore water pressure at two creeping landslides are explained by velocity-strengthening friction, in close agreement with laboratory measurements on similar materials. This suggests that the rate-strengthening friction commonly measured in clay-rich materials may govern episodic slow slip in landslides, in addition to tectonic faults. Further, our results show more generally that transient slow slip can arise in velocity-strengthening materials from modulation of effective normal stress through pore pressure fluctuations. This challenges the idea that apparently velocity-strengthening materials fail only by steady creep, and that transient slow slip phenomena require a specific and narrow range of extremely low stress and/or transitional frictional properties near the stability threshold.

Teaser

Measurements of velocity and water pressure in two slow landslides illuminate the mechanics of episodic slow frictional slip.

MAIN TEXT

Introduction

Landslides are triggered when shear stresses acting in the downhill direction are greater than or equal to the shear strength resisting sliding within a hillslope. Assuming Coulomb friction, this condition occurs when

$$\frac{\tau}{(\sigma+P)\mu+c'} \geq 1 \quad (1)$$

where τ is shear stress, σ is normal stress, P is pore fluid pressure (and σ-P is effective normal stress), μ is the static coefficient of friction (equivalent to tanϕ in soil mechanics, where ϕ is the friction angle), and c' is effective cohesion. For rainfall triggered landslides, as well as many coseismic landslides, failure is primarily controlled by the evolution of pore water pressure in both space (*1*, *2*) and time (*3*, *4*). In addition, coseismic landslides can occur due to transient increases in τ relative to (σ-P) resulting from the passage of seismic waves a (*5*).

As is the case for tectonic faulting and earthquakes, when the conditions in equation 1 are met, predicting whether landslide failure will occur catastrophically or by slow transient creep remains a basic, yet unresolved question in geomorphology and natural hazards research (*6*–*8*). At a fundamental level, this behavior is governed by the rheology of the slide material and failure plane; observations of landslide motion thus encode key information about the governing rheology. Mechanisms proposed to stabilize frictional sliding include clay swelling that increases lateral boundary friction during periods of high pore pressure (*9*); basal pore water pressure redistribution due to roughness (*10*); and perhaps most commonly the conceptual framework based on critical state soil mechanics that links stable (slow and quasi-continuous) landslide motion to shear-induced dilation of pore spaces. In this model, dilation reduces pore fluid pressure as sliding initiates, and hence increases effective normal stress and basal friction, serving to limit the slide's velocity by suppressing rapid runaway slip (*6*, *7*, *11*–*13*). Notably, dilatant strengthening has also been invoked to explain episodic slow slip events ("slow earthquakes") on tectonic faults (*14*) and along the beds of ice streams (*13*); however, in ice streams this process is arguably rare (*15*).

Rate-and-state friction is an empirically developed friction model that describes sliding friction in rock as well as a range of other materials, including some plastics, some metals, wood, and paper (*16*). The model, which is commonly applied to tectonic faults (*16*–*18*), provides a potentially powerful alternative approach to explain the rheology and predict the dynamics of landslides, including under what conditions rapid and catastrophic failure will occur (*8*, *19*–*21*). For example, a challenge with dilatant strengthening is that for the mm- to cm- wide localized shear zones typical of slow landslides (*22*–*24*), dilation can only operate over a slip length scale that is comparable to the shear zone thickness itself before a critical state porosity is reached and catastrophic failure occurs (*7*). Yet this length scale is often orders of magnitude smaller than the decimeter to meter-scale annual displacements that are typical of many slow landslides (*8*), which suggests that dilatant strengthening might not provide a universal explanation for stable frictional creep in these systems. Indeed, widely observed frictional creep in experiments on clay-rich sediments and fault gouges (*25*–*30*) and on the shallow reaches of tectonic faults at temperatures and effective stresses similar to landslides (*31*–*33*) demonstrates that stable frictional sliding is possible without necessarily appealing to a dilatancy-pore fluid pressure feedback.

Below we show that field-scale observations of sliding velocity and pore water pressure at two creeping landslides are explained by velocity-strengthening friction, in close agreement with laboratory measurements on similar materials. In the rate-and-state friction framework, the steady state coefficient of sliding friction, μ_{ss}, varies logarithmically with the sliding velocity, V:

$$\mu_{ss} = \frac{\tau}{(\sigma - P)} = \mu_0 + (a - b) ln\left(\frac{V}{V_o}\right) \quad (2)$$

where τ is shear stress, σ is normal stress, and P is pore fluid pressure (and σ-P is effective normal stress) *(16–18)*. In equation 2, (a-b) defines the rate-dependence of friction, and governs the sensitivity of the coefficient of sliding friction to the sliding velocity, V (normalized to a reference velocity, V_o). Individually, the parameter (a) governs the magnitude of a transient so-called "direct effect," in which the coefficient of sliding friction opposes acceleration due to dilation and a positive rate dependence of contact strength. The parameter (b), in turn, describes the so-called "evolution effect," which is interpreted to reflect the evolution of the real area of frictional contact (i.e. at grain boundaries or asperities) following a perturbation in velocity. Extensive experimental evidence shows that (a-b), which mathematically expresses the competition between the processes described above, can be either positive or negative, depending on rock type, accumulated shear strain, and temperature, among other factors *(16, 18, 25–30)*. In this framework, velocity-weakening, in which frictional resistance decreases with increasing sliding velocity and defined by negative values of (a - b), is a prerequisite for the nucleation of unstable slip *(16)*. In contrast, in materials characterized by velocity strengthening behavior, defined by positive values of (a - b), failure is thought to arise only by stable sliding or slow creep. From the perspective of landslide failure, the fact that rocks can exhibit either velocity-weakening or velocity-strengthening behavior provides a possible mechanism to differentiate bedrock landslides that accelerate catastrophically from those that exhibit apparently stable frictional sliding *(19)*. To the extent that this difference in behavior is governed by rock type *(25–29)*, it also suggests that it may be possible to predict which landslides are prone to catastrophic acceleration on the basis of geologic mapping and measurable material properties.

Few detailed observations exist to test whether models developed for fault friction can also be applied to landslides, or even to more generally define the rheology of landslide failure planes over relevant spatial and temporal scales. To date, a few studies have used a rate-and-state framework to explain observations of transient landslide motion *(19–21, 34)*. Ref *(8)* argued that the small size of landslides relative to the critical nucleation length for dynamic elastic rupture means that many landslides may slide stably despite velocity weakening friction, essentially representing the initiation of unstable failure, but which is unable to grow beyond a slow nucleation phase *(20)*. In support of this view, seismic tremor emanating from two patches on the base of the 2014 Askja caldera landslide prior to its catastrophic failure was interpreted to reflect velocity weakening patches on the bed of the landslide that were below the critical nucleation length for dynamic elastic rupture *(21)*. Alternatively, landslide deceleration in other settings following stress perturbations has been interpreted as evidence that (a - b) must be positive *(19, 34)*. Because all of these studies consider transient landslide dynamics in one way or another, they require independent fitting of at least three parameters: a, b, and D_c, the critical length-scale associated with refreshing frictional asperities, as well as in one case assumptions about the elastic properties of landslide materials *(20)*. Additionally, in two of the studies *(19, 34)* no information was available to constrain pore fluid pressures, requiring the further assumption of constant effective normal stress.

Slow Landslides as Field-Scale Rock Friction Experiments

Because many slow landslides undergo seasonal cycles of acceleration and deceleration that reveal tight coupling between pore pressure (and thus effective stress) and slide velocity - at low enough sliding velocities that inertial effects are negligible - treatment of these systems as steady-state failure is appropriate (31–34). At the same time, the large saturated hydraulic diffusivity (~ 10^{-4} m^2/s) (39–41) of many slow landslides, including Oak Ridge earthflow which we use in our analysis below, results in rapid (< 1 day) response times of landslide velocity (and hence basal effective stress) to rainfall induced pore fluid pressure pulses (39), suggesting that an assumption of hydrologic steady-state is also appropriate for the timescales considered here. For these reasons, here we adopt a steady-state perspective on landslide friction to investigate the role of rate-and-state frictional rheology in explaining their observed motion.

We solve for (a - b) in equation 2 directly, using displacement and pore fluid pressure measurements from two slow-moving landslides, Oak Ridge earthflow (39) and Minor Creek earthflow (42), in California's coast ranges. Constraints on both the shear and normal stress from field measurements (Materials and Methods) represent a novel opportunity to probe landslide frictional rheology, because they allow consideration of velocity as a function of the coefficient of sliding friction (or vice-versa; c.f. equation 2). Implicit in this treatment of the data is the fact that when in motion, the ratio $\tau/(\sigma\text{-P})$ at the slip surface represents the coefficient of sliding friction because the slip surface is at a state of failure and sliding. In comparison, in laboratory experiments designed to probe the frictional rheology of Earth materials, the dependence of shear strength on sliding velocity is typically investigated via a controlled velocity boundary condition and measurement of the resulting friction coefficient (18). Here, we treat the two landslides as field-scale experiments to obtain constraints on frictional behavior by approaching the problem in reverse - with variations in velocity driven by changes in $\tau/(\sigma\text{-P})$, and by measuring the corresponding sliding velocity.

Geologic and Geomorphic Setting

California's Franciscan mélange is an assemblage of variably deformed and metamorphosed rock units formed as part of the accretionary wedge in a subduction zone during the Mesozoic and early Cenozoic eras (43). Franciscan mélange is a block-in-matrix lithology, with a matrix of clay- and silt-stones containing blocks of more competent lithologies, including sandstone, chert, greenstone, and blueschist that range widely in size. The formation has been exhumed and uplifted in the California coast ranges, where it is well known for hosting slow landslides (23, 44). Soil cover is usually very thin (~10 cm) above the Franciscan mélange and its vadose zone structure is characterized by a thin (<3 m) seasonally unsaturated zone of weathered mudstone mélange overlying perennially saturated, unweathered mudstone mélange (39, 45). The matrix of the unweathered Franciscan mélange exhibits a combination of low shear strength, as constrained from laboratory determinations of drained shear strength from Oak Ridge earthflow's lateral shear margin (friction angle, $\Phi = 12°–14°$) (46) and low hydraulic conductivity, 10^{-6}–10^{-10} m/s, as constrained by slug tests at Minor Creek (42) and permeameter measurements at Oak Ridge (38). Details about the pore pressure and deformation monitoring for Minor Creek Earthflow are reported in (42) and outlined in the Materials and Methods. We use the basal pore pressure and deformation data from Minor Creek that are distilled in (7). Details about the pore pressure and deformation monitoring at Oak Ridge earthflow are reported in (39) and in the Materials and Methods. We use pore pressure data from a 2.5 m deep piezometer at Oak Ridge, and landslide displacement is quantified via extensometers and GPS. Figure 1A shows the network of GPS stations, extensometers, and the pore fluid pressure sensor used below, which is also described in more detail in the Materials and Methods.

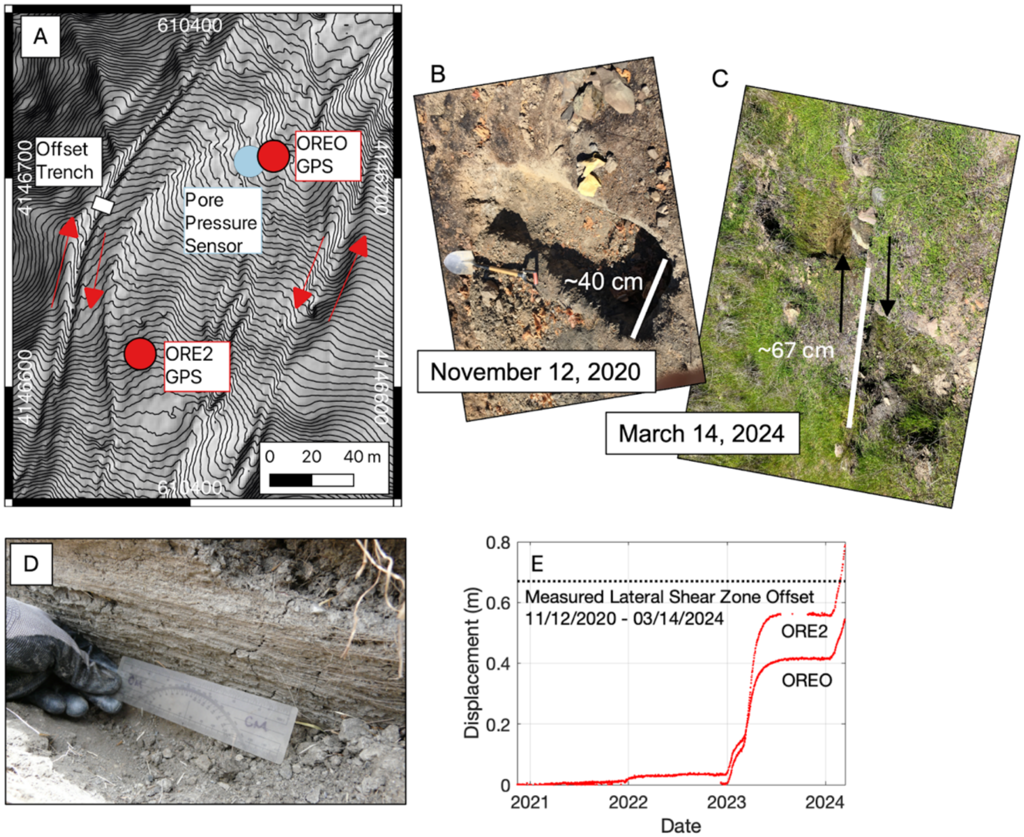

Fig. 1. Landslide Shear Zones and Localized Slip (A) 1-m LiDAR-derived contour map of the "transport zone" of Oak Ridge earthflow showing the placement of instrumentation used here. The white rectangle indicates the location of the photos in **(B)** and **(C)**. Coordinates are in UTM Zone 10N. **(B-C)** Offset of a trench excavated across the lateral shear margin at the location of the white rectangle between November 2020 and March 2024. **(D)** Offset measured in the hole **(C)** compared to measured GPS displacement upslope and downslope over the same time interval that is spanned by the photos in **(B)** and **(C)**. **(E)** Slickenlines observed along the western shear zone in spring, 2017.

Results

Slip Localization in Earthflow Shear Zones

Despite their name and appearance, earthflows like Oak Ridge and Minor Creek translate primarily via sliding along discrete failure surfaces rather than through internal deformation *(9, 22, 23)*. We provide specific evidence of this localization from Oak Ridge earthflow, as a well-studied example. Figures 1B-C show a ~ 0.4 m wide trench excavated across the western lateral shear margin of Oak Ridge in November, 2020 that recorded ~ 0.67 m of offset as of April, 2024 along a narrow band that is typical of observations of earthflow sliding at other locations *(22, 23)*. The trench is located downslope of the OREO GPS antenna and upslope of the ORE2 GPS antenna, respectively (Figure 1A). The magnitude of recorded offset in the trench is bracketed by the displacement measured at the two GPS stations over the time interval spanned by the photos in B and C, ~ 0.54 m at OREO and 0.79 m at ORE2 (Figure 1D), illustrating that all of the displacement measured in the landslide center can be accounted for within the offset observed along the narrow lateral shear margin. Finally, evidence for localization is also apparent from slickenlines observed along the same shear zone (Figure 1E) shown in Figure 1C. In further support of shear localization at Oak Ridge, comparison of extensometers that span the western shear margin to the internal GPS antennas in parallel positions (OREO and ORE2) show similar magnitude and timing of displacement (47). In summary, field observations and geodetic measurements show that there is little internal deformation currently observed within Oak Ridge earthflow. Rather, deformation is localized along a thin shear zone. While our observations do not directly constrain basal landslide deformation, the close agreement of lateral and internal displacement (Figure 1B-E) suggests that the lateral shear margin is continuous with the basal shear zone, which is only 8-10 m below the surface (38). This interpretation is also supported by electrical resistivity tomography at Oak Ridge (38).

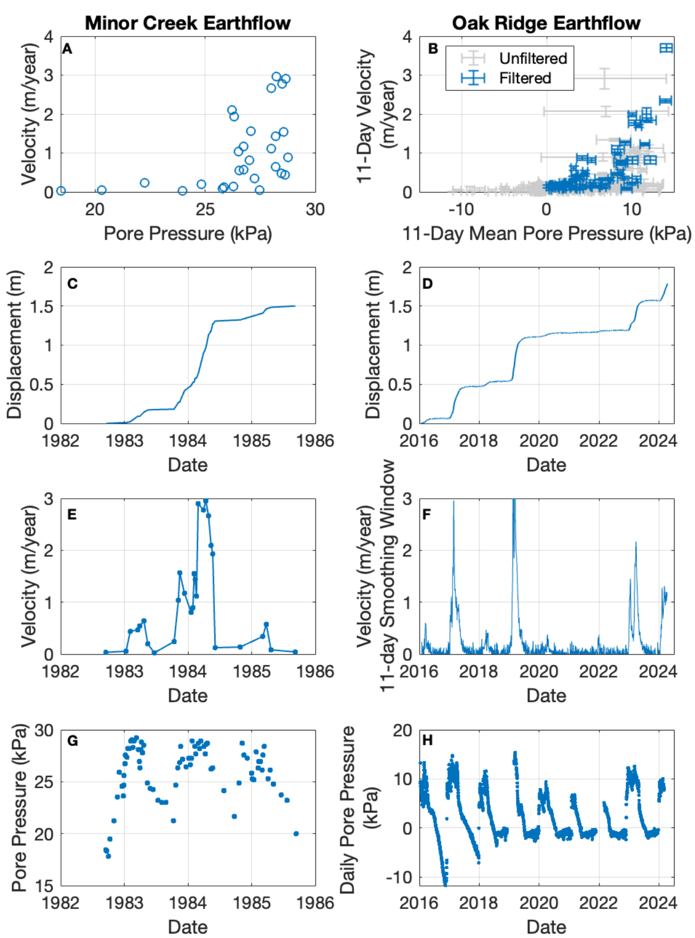

Fig. 2. Seasonal landslide slow slip events driven by pore fluid pressure (A) Estimated shear zone pore pressure, **(C)** Extensometer displacement, **(E)** Velocity, and **(G)** velocity as a function of pore fluid pressure for Minor Creek earthflow from 1982-1986. **(B)** Velocity averaged over a 10-day window versus 10-day mean pore pressure at 2.5 m depth for Oak Ridge earthflow. The error bars represent the standard error for the calculated velocity and the standard deviation of the 10-day mean pore pressure, respectively. The gray points represent those data points that were discarded in our analysis because either the estimated velocity was less than twice the standard error on the velocity or the pressure recorded was negative, as described in detail in Methods and Materials. **(D)** GPS-derived horizontal displacement, **(F)** Horizontal velocity calculated over a 10 day window, and **(H)** daily pore pressure at 2.5 m depth for Oak Ridge earthflow from 2016-2023.

Seasonal Slow Landslide Slip Events

Fig. 2 shows temporal patterns of pore pressure (C, D), displacement (D, E), and velocity (F, G) for the Minor Creek and Oak Ridge earthflows. Landslide displacement episodes are highly seasonal at each location (Fig. 2, B to E), and are driven by winter increases in pore fluid pressure (Fig. 2, A and B) in California's Mediterranean climate where rainfall is concentrated from November to April. The velocity of both slides varies systematically and non-linearly with pore pressure (Fig. 1, A and B), as has been observed at Oak Ridge earthflow *(38)*, as well as at other slow moving landslides *(35–37)*. This observation embeds information about the rheology that controls slide motion - and particularly its dependence on effective stress as modulated by pore pressure.

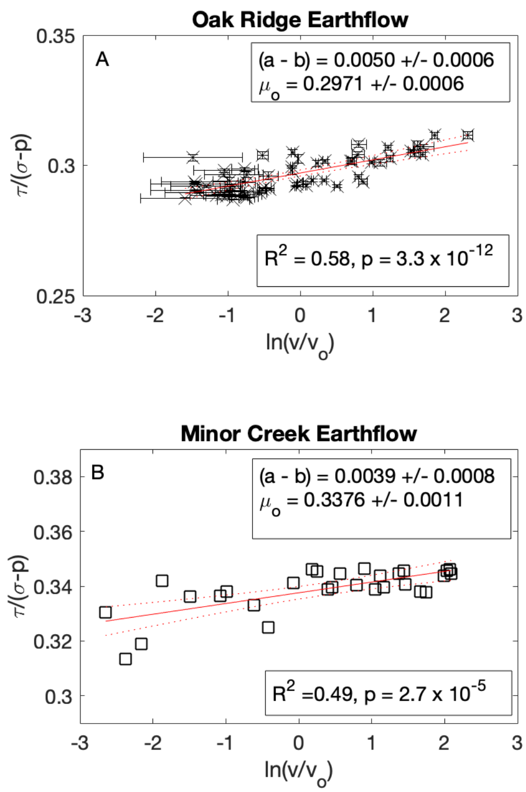

Fig. 3. Sensitivity of landslide friction to velocity. Ratio of shear stress to effective normal stress (ss) plotted as a function of the natural log of landslide velocity normalized by a reference velocity, ln(V/Vo), for **(A)** Oak Ridge earthflow and **(B)** Minor Creek earthflow. The error bars for the effective stress reflect +/- 1 standard deviation of the daily pore pressure measured during the 10-day window over which velocity was measured. Similarly, the uncertainty in velocity reflects the standard error on the slope of the linear regression to the GPS-derived horizontal displacement over the 10-day averaging window. For Minor Creek, velocities are computed for every measurement of displacement. Regression lines (solid red) and 95% confidence intervals (dotted red) are shown in both **(A)** and **(B)**. V_o in both A and B is 1 m/yr.

Velocity Dependence of Landslide Friction

In Fig. 3 we provide an assessment of the suitability of the rate-and-state formulation in describing the field observations, and define the velocity dependence via solution of equation 1 through linear regression of steady-state landslide friction at the two locations. Fig 3. shows that the data are well-fit with equation 1 (Minor Creek: R^2 = 0.49, p = 2.8 x

10^{-5}; Oak Ridge: R^2 = 0.58, p = 3.3 x 10-12) and exhibit (within uncertainty) nearly identical velocity-strengthening behavior. *(a - b)* = 0.0050 +/- 0.0006 at Oak Ridge and 0.0039 +/- 0.0008 at Minor Creek.

Discussion

Rate-and-State Friction as a Prospective Mechanism to Explain Frictional Creep in Slow Landslides

In the Coast Ranges of California, the seasonal dynamics of slow landslides are strongly correlated *(48, 49)*. Because the apparent velocity sensitivity of friction at Oak Ridge earthflow and Minor Creek earthflow is also nearly identical, it is natural to ask if velocity-strengthening rate-and-state friction provides a mechanism to explain the widespread, correlated landslide creep observed within the clay-rich exhumed subduction mélange in California. The observation that the data in Fig. 3 (A and B) are well fit with a linear relationship, by itself, suggests that the answer to this question is yes. In contrast, the steady-state dilatant strengthening model *(7)* predicts a linear relationship between shear zone pore fluid pressure and sliding velocity, a relationship that is not supported by the data (Fig. 1 G and H Fig. 2 A and B).

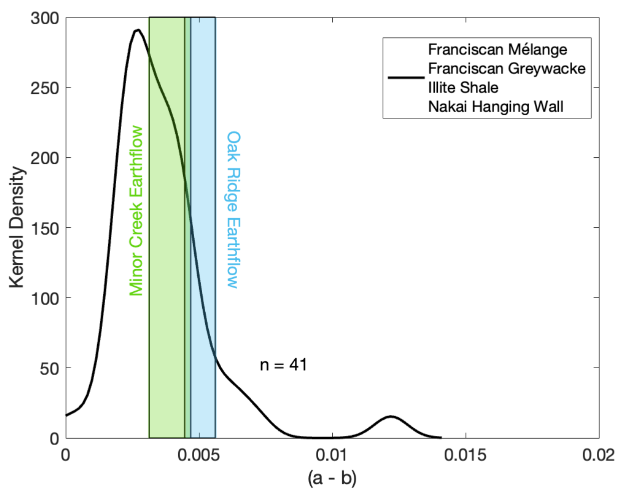

Fig. 4. Comparison of field-derived and experimentally derived friction. (*a* - *b*) calculated for Oak Ridge and Minor Creek earthflows in Figure 3 compared to 17 laboratory determinations of (*a* - *b*) for Franciscan mélange *(50, 51)*, Franciscan Graywacke*(50)*, Illite Shale*(25)*, and hanging wall mudstones from the Nankai subduction zone *(52)*.

Comparing Landslide Friction to Laboratory Measurements of Fault Friction in Similar Rock Types

A further and arguably more compelling test of whether rate-and-state friction governs the velocity strengthening behavior of Oak Ridge earthflow and Minor Creek earthflow is to compare the fits of (*a* - *b*) in Fig. 3 (A and B) to experimental rock friction data for the same and similar lithologies. We focus our comparisons on low-temperature friction experiments performed on Franciscan mélange and on rocks and marine sediments that are compositionally similar to the clay-rich mélange matrix. Because slow landslide motion more generally is associated with clay rich rocks *(8)*, experimental friction data from relevant, and similar, clay-rich lithologies may also provide insight into the rheology of slow landslides elsewhere. Figure 4 shows that the values of (a - b) that we fit in Fig. 3 are statistically indistinguishable from values of (a - b) from room-temperature rock friction experiments on Franciscan mélange (*50, 51*), Franciscan graywacke (*50*), illitic shale (*25*), and hanging wall mudstones from the Nankai subduction zone that represent a modern environment analogous to the Franciscan matrix of the Coast Ranges (*52*).

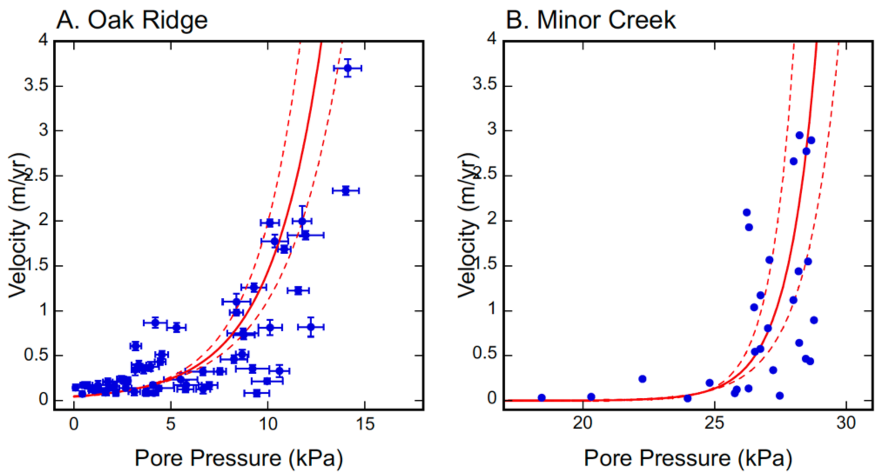

Figure 5. Modulation of velocity by pore fluid pressure. Velocity versus pore fluid pressure at **(A)** Oak Ridge and **(B)** Minor Creek earthflows along with the relationship between those variables obtained from solving the fit to equation 1 for velocity and then plotting as a function of pore fluid pressure. Uncertainty envelopes reflect propagation of the uncertainties in *(a - b)* and μ_o from the fits shown in **Fig. 3**.

Slow Landslides as Episodic Slow Slip Events in which Velocity is Modulated by Pore Fluid Pressure

Significantly, our results show that transient - but slow - slip may arise in velocity strengthening materials simply due to modulation of the effective normal stress via pore pressure fluctuations. This fact is clearly demonstrated by solving equation 2 for velocity and then plotting predicted and observed velocity for Oak Ridge and Minor Creek earthflows as a function of pore fluid pressure (Fig. 5, A and B). The strong coupling between velocity and pore pressure observed and predicted by velocity-strengthening friction at both Minor Creek and Oak Ridge earthflows contrasts with the widely held idea that apparently velocity-strengthening materials can only fail by steady creep - and therefore that emergent slow creep transients, including slow slip events and associated slow earthquake phenomena observed in a wide range of settings globally fundamentally require a specific and narrow range of extremely low stress and/or transitional frictional properties near the stability threshold, and/or pore fluid pressure feedbacks that suppress acceleration to rapid slip (e.g., *14, 53, 54*).

In previous work, asynchronous stick-slip events recently observed at small scales within Oak Ridge earthflow were interpreted as arising from failure of small velocity-weakening patches that are loaded elastically by motion of a surrounding velocity strengthening shear zone (*47*), a mechanism similar to that proposed for tremor that accompanies slow slip events on tectonic faults (*55*). Our results support this interpretation of slip plane processes by demonstrating that the bulk (effective) frictional behavior of Franciscan mélange at the field scale is well-explained with rate-strengthening friction, as also documented in laboratory friction measurements of both the mélange matrix and clay-rich lithologies more generally. This is strikingly similar to the paired observations of emergent shallow slow slip events associated with tremor in modern subduction zones (*33*, *55*), and laboratory frictional properties indicating velocity strengthening behavior of relevant fault rocks and protolith sediments in these environments (*52*, *55*).

Finally, we acknowledge that while the simple rate-state formulation provides a good fit to the data from Oak Ridge and Minor Creek and thus provides a viable mechanism to explain the observed creeping behavior and dependence on pore fluid pressure, the fit is not perfect. An obvious limitation of our data, and one that could easily explain the observed scatter, is the fact that our measurements of pore fluid pressure reflect point measurements that may not perfectly capture the average pore pressure conditions at the scale of the entire landslide mass. While investigating this and other potential sources of the scatter in the relationship between velocity and pore fluid pressure observed at Oak Ridge and Minor Creek is a worthy goal, it remains beyond the scope of the current work, which aims to investigate the first-order patterns in the relationship between pore fluid pressure and velocity that is apparent in Figure 5 and Figure 2.

Implications for Predicting Landslide Hazard

Our results also provide a physically-based and experimentally verifiable explanation for landslide creep. In short, the inherently rate strengthening behavior of clay-rich shear zones (e.g., *25*) can explain the behavior of slow landslides developed in Franciscan mélange. This suggests that it may be possible to predict which landslides are prone to catastrophic acceleration on the basis of paired geologic mapping and laboratory measurements of material properties. For example, creeping landslides revealed by synthetic aperture radar interferometry (InSAR) in the western U.S. are commonly associated with surface exposures of clay-rich subduction mélange (*48*, *49*). Where these rocks transition to quartz-rich turbiditic sandstones to the north, evidence for creeping landslides largely disappears, although evidence for landsliding is still ubiquitous in the topography (*56*). This potential lithologic control on the style of landslide failure is striking and raises the possibility that fundamental differences in landslide behavior - and hazard - in these two settings could be controlled by the frictional properties of the contrasting lithologies in the two settings, a hypothesis which is eminently testable through targeted experiments.

Materials and Methods

Deformation Monitoring

Deformation monitoring at Oak Ridge for this study consists of two Trimble NetR9 GPS receivers with Zephyr antennas bolted to large boulders spaced ~100 m apart along the axis of the most active part of the slide (Figure 1A). GPS data are telemetered to and first processed by Earthscope Consortium and then subsequently post-processed at the Nevada Geodetic Laboratory (*57*). We use locations in the IGS14 reference frame, which we convert to daily landslide displacement by removing horizontal plate tectonic motion in the IGS14 reference frame by using data from a nearby permanent GPS station (P227) installed on a stable slope on the same side of the actively creeping Calaveras fault as Oak Ridge earthflow.

Pore Pressure Monitoring

Our pore pressure measurements come from a grouted vibrating-wire piezometers (RST Instruments, model VW2100-0.07) colocated with the OREO GPS antenna, at a depth of 2.5 m (Figure 1A). Piezometer accuracy is 0.07 kPa with a precision of 0.0175 kPa. Piezometer readings, collected every 10 min, were corrected for changes in ground temperature via a calibration from the manufacturer. The landslide failure planes at Oak Ridge and Minor Creek are perennially saturated, however landslide motion at both locations occurs only when the water table rises close to the ground surface and the entire landslide body above the failure plane is also near saturation (39, 42). At Oak Ridge earthflow, high temporal resolution monitoring of pore pressure and landslide motion reveals that when the landslide body is near saturation, pore fluid pressure pulses travel to the base of the ~ 8 m landslide nearly instantaneously, with no observable lag or attenuation, and cause landslide acceleration within ~ 1 day of rainfall events (39). This implies a relatively large hydraulic diffusivity of the slide mass and shear zone together (~ 10^{-4} m^2/s) and a well-connected hydrogeologic system, and indicates that piezometers at intermediate depths in the landslide constrain the amplitude of pressure pulses that reach the landslide shear zone. For this reason, we use pore pressure data for Oak Ridge earthflow from a 2.5 m depth vibrating wire piezometer that correlates strongly with the GPS-derived velocity (39). For Minor Creek we use the basal pore pressure record inferred in (7) directly, which also comes from an intermediate depth piezometer.

Calculating the Ratio of Shear Stress to Effective Normal Stress, $\frac{\tau}{(\sigma - P)}$

Because motion of the landslide occurs close to saturated conditions, we follow (7) and do not attempt to model the accretion of a water table, but instead assume all changes in pore fluid pressure at the landslide shear zone base are related to pulses of pore fluid pressure that are generated at the landslide surface and propagate vertically (39). Accordingly, the ratio of shear stress, τ, to effective normal stress, (σ - P), at the base of Oak Ridge earthflow (the left hand side of equation 2), is given by:

$$\frac{\tau}{(\sigma - P)} = \frac{\rho_{sat} g h \sin\theta}{(\rho_{sat} g h \cos\theta - P)} \qquad (3)$$

where ρ_{sat} is the saturated density of the landslide, is the slope of the landslide failure surface, h is the depth of the landslide, and P is pore fluid pressure in the landslide shear zone.

We use the OREO GPS antenna (39) to calculate the 3D displacement and velocity for Oak Ridge earthflow between 2016 and 2024. We experimented with different time windows for calculating velocity from daily displacement, and ultimately settled on a window of 11 days, which provides a compromise between the noise inherent in GPS velocity obtained over shorter time intervals, and smoothing of the real temporal variability of interest to this study over longer time intervals. Additionally, we discarded velocity estimates where the estimated velocity was less than twice the standard error on the velocity calculated over 11-days. We also discarded data points with either negative velocities or negative pore pressures that reflect matric suction under conditions of low moisture content when the piezometer is above the water table and the pore fluid pressure is therefore poorly constrained (39). This condition only occurs during the summer when the landslide is not active (Fig. 2B,D,F,G). Finally, we discarded points where the pore pressure changed substantially during the 11-day window over which velocity was calculated, as a large change in pore pressure is not consistent with the steady-state assumption in equation 2. We selected a cutoff of 1 kPa for an acceptable standard deviation of pore pressure within the 11-day window. Figure 2B shows the relationship between pore fluid pressure and velocity for the windowed data before and after the above filtering exercise.

For each filtered velocity measurement, we then calculated the standard deviation of the measured pore pressure within the 11-day window, which we propagated through the calculation of equation 3 in order to place uncertainty bounds on reported values of *(-P)*. For Minor Creek we use measurements of displacement that were made 21 times over 3 years between 1982 and 1985 using wire line extensometers *(42)*. Table S1 provides the data required to calculate equation 3, along with pore pressure (Table S2, S3), for both Minor Creek earthflow and Oak Ridge earthflow.

References

1. J. P. Perkins, M. E. Reid, K. M. Schmidt, Control of landslide volume and hazard by glacial stratigraphic architecture, northwest Washington State, USA. *Geology* **45**, 1139–1142 (2017).

2. M. E. Reid, R. M. Iverson, Gravity-driven groundwater flow and slope failure potential: 2. Effects of slope morphology, material properties, and hydraulic heterogeneity. *Water Resour. Res.* **28**, 939–950 (1992).

3. R. M. Iverson, Landslide triggering by rain infiltration. *Water Resour. Res.* **36**, 1897–1910 (2000).

4. M. E. Reid, A Pore-Pressure Diffusion Model for Estimating Landslide-Inducing Rainfall. *J. Geol.* **102**, 709–717 (1994).

5. N. M. Newmark, Effects of Earthquakes on Dams and Embankments. *Géotechnique* **15**, 139–160 (1965).

6. R. M. Iverson, M. E. Reid, N. R. Iverson, R. G. LaHusen, M. Logan, J. E. Mann, D. L. Brien, Acute sensitivity of landslide rates to initial soil porosity. *Science* **290**, 513–516 (2000).

7. R. M. Iverson, Regulation of landslide motion by dilatancy and pore pressure feedback. *J. Geophys. Res.* **110**, F02015 (2005).

8. P. Lacroix, A. L. Handwerger, G. Bièvre, Life and death of slow-moving landslides. *Nat. Rev. Earth Environ*. **1**, 404–419 (2020).

9. W. H. Schulz, J. B. Smith, G. Wang, Y. Jiang, J. J. Roering, Clayey Landslide Initiation and Acceleration Strongly Modulated by Soil Swelling. *Geophys. Res. Lett.* **45**, 1888–1896 (2018).

10. R. L. Baum, A. M. Johnson, Steady movement of landslides in fine-grained soils: a model for sliding over an irregular slip surface. Landslide Process. Utah Obs. Theory (1993).

11. F. Agliardi, M. M. Scuderi, N. Fusi, C. Collettini, Slow-to-fast transition of giant creeping rockslides modulated by undrained loading in basal shear zones. *Nat. Commun.* **11**, 1–11 (2020).

12. J. M. Carey, C. I. Massey, B. Lyndsell, D. N. Petley, Displacement mechanisms of slow-moving landslides in response to changes in porewater pressure and dynamic stress. *Earth Surf. Dyn.* **7**, 707–722 (2019).

13. P. L. Moore, N. R. Iverson, Slow episodic shear of granular materials regulated by dilatant strengthening. *Geology* **30**, 843–846 (2002).

14. P. Segall, A. M. Rubin, A. M. Bradley, J. R. Rice, Dilatant strengthening as a mechanism for slow slip events. *J. Geophys. Res. Solid Earth* **115** (2010).

15. N. R. Iverson, Shear resistance and continuity of subglacial till: hydrology rules. *J. Glaciol.* **56**, 1104–1114 (2010).

16. C. H. Scholz, Earthquakes and friction laws. *Nature* **391**, 37–42 (1998).

17. J. H. Dieterich, "A Model for the Nucleation of Earthquake Slip" in Earthquake Source Mechanics (American Geophysical Union (AGU), 1986; https://onlinelibrary.wiley.com/doi/abs/10.1029/GM037p0037), pp. 37–47.

18. C. Marone, Laboratory-Derived Friction Laws and Their Application to Seismic Faulting. *Annu. Rev. Earth Planet. Sci.* **26**, 643–696 (1998).

19. A. Helmstetter, D. Sornette, J.-R. Grasso, J. V. Andersen, S. Gluzman, V. Pisarenko, Slider block friction model for landslides: Application to Vaiont and La Clapière landslides. *J. Geophys. Res. Solid Earth* **109** (2004).

20. A. L. Handwerger, A. W. Rempel, R. M. Skarbek, J. J. Roering, G. E. Hilley, Rate-weakening friction characterizes both slow sliding and catastrophic failure of landslides. *Proc. Natl. Acad. Sci.* **113**, 10281–10286 (2016).

21. A. Schöpa, W.-A. Chao, B. P. Lipovsky, N. Hovius, R. S. White, R. G. Green, J. M. Turowski, Dynamics of the Askja caldera July 2014 landslide, Iceland, from seismic signal analysis: precursor, motion and aftermath. *Earth Surf. Dyn.* **6**, 467–485 (2018).

22. D. K. Keefer, A. M. Johnson, "Earth flows; morphology, mobilization, and movement" (USGS Numbered Series 1264, U.S. G.P.O., 1983); http://pubs.er.usgs.gov/publication/pp1264.

23. B. H. Mackey, J. J. Roering, Sediment yield, spatial characteristics, and the long-term evolution of active earthflows determined from airborne LiDAR and historical aerial photographs, Eel River, California. *GSA Bull.* **123**, 1560–1576 (2011).

24. A. L. Nereson, N. J. Finnegan, Drivers of earthflow motion revealed by an 80 yr record of displacement from Oak Ridge earthflow, Diablo Range, California, USA. *GSA Bull.* **131**, 389–402 (2019).

25. M. J. Ikari, D. M. Saffer, C. Marone, Frictional and hydrologic properties of clay-rich fault gouge. *J. Geophys. Res. Solid Earth* **114**, B05409 (2009).

26. M. J. Ikari, C. Marone, D. M. Saffer, On the relation between fault strength and frictional stability. *Geology* **39**, 83–86 (2011).

27. M. J. Ikari, D. M. Saffer, C. Marone, Effect of hydration state on the frictional properties of montmorillonite-based fault gouge. *J. Geophys. Res. Solid Earth* **112** (2007).

28. B. M. Carpenter, C. Marone, D. M. Saffer, Weakness of the San Andreas Fault revealed by samples from the active fault zone. *Nat. Geosci.* **4**, 251–254 (2011).

29. B. M. Carpenter, D. M. Saffer, C. Marone, Frictional properties and sliding stability of the San Andreas fault from deep drill core. *Geology* **40**, 759–762 (2012).

30. D. R. Faulkner, T. M. Mitchell, J. Behnsen, T. Hirose, T. Shimamoto, Stuck in the mud? Earthquake nucleation and propagation through accretionary forearcs. *Geophys. Res. Lett.* **38** (2011).

31. A. T. Linde, M. T. Gladwin, M. J. S. Johnston, R. L. Gwyther, R. G. Bilham, A slow earthquake sequence on the San Andreas fault. *Nature* **383**, 65–68 (1996).

32. L. M. Wallace, S. C. Webb, Y. Ito, K. Mochizuki, R. Hino, S. Henrys, S. Y. Schwartz, A. F. Sheehan, Slow slip near the trench at the Hikurangi subduction zone, New Zealand. *Science* **352**, 701–704 (2016).

33. E. Araki, D. M. Saffer, A. J. Kopf, L. M. Wallace, T. Kimura, Y. Machida, S. Ide, E. Davis, IODP EXPEDITION 365 SHIPBOARD SCIENTISTS, Recurring and triggered slow-slip events near the trench at the Nankai Trough subduction megathrust. *Science* **356**, 1157–1160 (2017).

34. P. Lacroix, H. Perfettini, E. Taipe, B. Guillier, Coseismic and postseismic motion of a landslide: Observations, modeling, and analogy with tectonic faults. *Geophys. Res. Lett.* 41, 6676–6680 (2014).

35. J.-P. Malet, O. Maquaire, E. Calais, The use of Global Positioning System techniques for the continuous monitoring of landslides: application to the Super-Sauze earthflow (Alpes-de-Haute-Provence, France). *Geomorphology* **43**, 33–54 (2002).

36. J. A. Coe, W. L. Ellis, J. W. Godt, W. Z. Savage, J. E. Savage, J. A. Michael, J. D. Kibler, P. S. Powers, D. J. Lidke, S. Debray, Seasonal movement of the Slumgullion landslide determined from Global Positioning System surveys and field instrumentation, July 1998–March 2002. *Eng. Geol.* **68**, 67–101 (2003).

37. J. Corominas, J. Moya, A. Ledesma, A. Lloret, J. A. Gili, Prediction of ground displacements and velocities from groundwater level changes at the Vallcebre landslide (Eastern Pyrenees, Spain). *Landslides* **2**, 83–96 (2005).

38. C. R. Murphy, N. J. Finnegan, F. K. J. Oberle, Vadose Zone Thickness Limits Pore-Fluid Pressure Rise in a Large, Slow-Moving Earthflow. *J. Geophys. Res. Earth Surf.* **127**, e2021JF006415 (2022).

39. N. J. Finnegan, J. P. Perkins, A. L. Nereson, A. L. Handwerger, Unsaturated Flow Processes and the Onset of Seasonal Deformation in Slow-Moving Landslides. J. *Geophys. Res. Earth Surf*. **126**, e2020JF005758 (2021).

40. M. Berti, A. Simoni, Field evidence of pore pressure diffusion in clayey soils prone to landsliding. *J. Geophys. Res. Earth Surf.* **115** (2010).

41. R. L. Baum, M. E. Reid, "Geology, hydrology and mechanics of the Alani-Paty Landslide, Manoa Valley, Oahu, Hawaii" (92–501, U.S. Geological Survey, 1992); https://doi.org/10.3133/ofr92501.

42. R. M. Iverson, J. J. Major, Rainfall, ground-water flow, and seasonal movement at Minor Creek landslide, northwestern California: Physical interpretation of empirical relations. *GSA Bull.* **99**, 579–594 (1987).

43. J. Wakabayashi, Anatomy of a subduction complex: architecture of the Franciscan Complex, California, at multiple length and time scales. *Int. Geol. Rev.* **57**, 669–746 (2015).

44. H. M. Kelsey, Earthflows in Franciscan melange, Van Duzen River basin, California. *Geology* **6**, 361–364 (1978).

45. W. J. Hahm, D. M. Rempe, D. N. Dralle, T. E. Dawson, S. M. Lovill, A. B. Bryk, D. L. Bish, J. Schieber, W. E. Dietrich, Lithologically Controlled Subsurface Critical Zone Thickness and Water Storage Capacity Determine Regional Plant Community Composition. *Water Resour. Res.* **55**, 3028–3055 (2019).

46. A. L. Nereson, S. D. Olivera, N. J. Finnegan, Field and Remote-Sensing Evidence for Hydro-mechanical Isolation of a Long-Lived Earthflow in Central California. *Geophys. Res. Lett.* **45**, 9672–9680 (2018).

47. N. J. Finnegan, E. E. Brodsky, H. M. Savage, A. L. Nereson, C. R. Murphy, Seasonal Slow Landslide Displacement Is Accommodated by mm-Scale Stick-Slip Events. *Geophys. Res. Lett.* **49**, e2022GL099548 (2022).

48. A. L. Handwerger, E. J. Fielding, S. S. Sangha, D. P. S. Bekaert, Landslide Sensitivity and Response to Precipitation Changes in Wet and Dry Climates. *Geophys. Res. Lett.* **49**, e2022GL099499 (2022).

49. Y. Xu, W. H. Schulz, Z. Lu, J. Kim, K. Baxstrom, Geologic controls of slow-moving landslides near the US West Coast. *Landslides* **18**, 3353–3365 (2021).

50. C. A. Morrow, D. E. Moore, D. A. Lockner, "Dependence of frictional strength on compositional variations of Hayward fault rock gouges" (2010–1184, U.S. Geological Survey, 2010); https://doi.org/10.3133/ofr20101184.

51. D. E. Moore, D. A. Lockner, S. Hickman, Hydrothermal frictional strengths of rock and mineral samples relevant to the creeping section of the San Andreas Fault. *J. Struct. Geol.* **89**, 153–167 (2016).

52. M. J. Ikari, D. M. Saffer, Comparison of frictional strength and velocity dependence between fault zones in the Nankai accretionary complex. *Geochem. Geophys. Geosystems* **12** (2011).

53. R. M. Skarbek, A. W. Rempel, D. A. Schmidt, Geologic heterogeneity can produce aseismic slip transients. *Geophys. Res. Lett.* **39**, L21306 (2012).

54. A. M. Rubin, Episodic slow slip events and rate-and-state friction. *J. Geophys. Res. Solid Earth* **113** (2008).

55. R. Bürgmann, The geophysics, geology and mechanics of slow fault slip. *Earth Planet. Sci. Lett.* **495**, 112–134 (2018).

56. J. J. Roering, J. W. Kirchner, W. E. Dietrich, Characterizing structural and lithologic controls on deep-seated landsliding: Implications for topographic relief and landscape evolution in the Oregon Coast Range, USA. *GSA Bull*. **117**, 654–668 (2005).

57. G. Blewitt, W. C. Hammond, C. Kreemer, Harnessing the GPS Data Explosion for Interdisciplinary *Science*. doi: 10.1029/2018eo104623 (2018).

Acknowledgments

Funding:

National Science Foundation grant EAR-1658800 (NJF)

National Science Foundation grant EAR-2222149 (NJF)

Author contributions:

Conceptualization: NJF,DMA

Methodology: NJF,DMA
Investigation: NJF,DMA
Visualization: NJF,DMA
Writing – original draft: NJF,DMA
Writing – review & editing: NJF,DMA

Competing interests: Authors declare that they have no competing interests.

Data and materials availability: All data are available in the main text, the supplementary materials, or at https://doi.org/10.5281/zenodo.11511667

Supplementary Materials

	Minor Creek Earthflow (42)	*Oak Ridge Earthflow* (38, 39, 46)
Slope Angle (θ)	15°	16°
Depth (h)	6 m	8 m
Length	~ 800 m	~ 1400 m
Saturated Density ($\boldsymbol{\rho}_s$)	2234 kg/m^3	2344 kg/m^3

Table S1. Representative landslide data required to calculate equation 3.

Time (Yr)	Pore Pressure (Pa)	Standard Deviation of Pressure in 11-day window (Pa)	11-Day Velocity (m/yr)	Velocity Standard Error (m/yr) from 11-day velocity regression	τ (Pa)	σ (Pa)	V_o (m/yr)
2016.293	5506.1681	850.95265	0.24	0.07	50654	176650	0.365
2016.3231	4074.8454	140.70372	0.17	0.03	50654	176650	
2017.1362	11763.439	493.74124	1.99	0.17	50654	176650	
2017.1663	10344.624	686.35347	1.77	0.07	50654	176650	
2017.1964	11563.612	539.80861	1.23	0.04	50654	176650	
2017.2567	12210.198	657.07856	0.82	0.11	50654	176650	
2017.3169	5288.3887	479.08435	0.81	0.05	50654	176650	
2017.347	4532.8557	330.44291	0.51	0.05	50654	176650	
2017.3771	3598.1666	390.63147	0.35	0.04	50654	176650	
2017.4073	2782.3341	137.07018	0.22	0.04	50654	176650	
2017.4374	2166.8649	136.79925	0.09	0.04	50654	176650	
2017.4675	2094.6913	110.46031	0.16	0.05	50654	176650	
2017.4976	1641.2532	167.09028	0.09	0.03	50654	176650	

2017.5277	1246.7787	170.13634	0.12	0.03	50654	176650		
2017.5578	903.89059	162.50742	0.13	0.04	50654	176650		
2017.588	439.23392	134.17581	0.07	0.03	50654	176650		
2018.1903	9955.2118	809.87089	0.22	0.03	50654	176650		
2018.2505	9428.3844	646.19212	0.08	0.04	50654	176650		
2018.2806	6653.611	917.77125	0.33	0.04	50654	176650		
2018.3107	4385.4653	793.36786	0.14	0.03	50654	176650		
2018.3409	3112.7008	301.60347	0.1	0.04	50654	176650		
2018.371	2675.7159	310.89662	0.14	0.02	50654	176650		
2018.4011	1793.9303	425.4448	0.14	0.03	50654	176650		
2019.1841	14114.085	708.4386	3.7	0.1	50654	176650		
2019.2142	14013.232	665.49006	2.34	0.05	50654	176650		
2019.2444	11950.3	936.71929	1.84	0.05	50654	176650		
2019.3046	4200.5036	602.70801	0.87	0.06	50654	176650		
2019.3347	3185.1506	284.45284	0.61	0.05	50654	176650		
2019.3648	3955.962	425.85893	0.38	0.05	50654	176650		
2019.3949	4458.327	276.85629	0.43	0.04	50654	176650		
2019.4251	3171.1955	205.89278	0.34	0.06	50654	176650		
2019.4552	2539.4832	309.75788	0.22	0.02	50654	176650		
2019.4853	1240.1119	480.11571	0.17	0.05	50654	176650		
2020.0575	6984.7482	408.15175	0.17	0.04	50654	176650		
2020.0876	5759.8627	418.91593	0.13	0.03	50654	176650		
2020.2081	6664.8487	357.24831	0.13	0.05	50654	176650		
2020.2683	7527.3116	310.30553	0.33	0.04	50654	176650		
2020.2984	5789.9162	649.28281	0.17	0.05	50654	176650		
2020.3285	4129.9124	222.92302	0.08	0.03	50654	176650		
2020.3587	3731.5104	193.23522	0.09	0.04	50654	176650		
2020.5092	695.0626	266.51976	0.17	0.04	50654	176650		
2023.0609	10116.18	616.17547	0.81	0.09	50654	176650		
2023.091	8672.0601	334.06437	0.51	0.05	50654	176650		
2023.1211	9207.034	875.5668	0.35	0.04	50654	176650		
2023.1513	10591.415	519.35012	0.33	0.07	50654	176650		
2023.2115	10842.411	333.2371	1.69	0.04	50654	176650		
2023.2416	10102.199	462.95184	1.98	0.04	50654	176650		

2023.2717	9276.8537	648.85229	1.26	0.05	50654	176650	
2023.3018	8759.8326	547.15927	0.73	0.05	50654	176650	
2023.3621	3349.72	370.99109	0.4	0.05	50654	176650	
2023.3922	2463.141	238.08177	0.24	0.03	50654	176650	
2023.4223	1755.1309	242.67502	0.21	0.04	50654	176650	
2023.4524	1080.1784	284.48491	0.12	0.04	50654	176650	
2023.4853	464.10383	113.61663	0.17	0.03	50654	176650	
2023.5154	87.357556	116.19436	0.15	0.04	50654	176650	
2024.0684	8253.8141	696.05004	0.46	0.04	50654	176650	
2024.0986	8387.0751	712.1681	1.1	0.09	50654	176650	
2024.1287	8715.2651	806.32901	0.75	0.06	50654	176650	
2024.1588	8385.133	340.92015	0.98	0.04	50654	176650	

Table S2. Pore pressure and displacement data for Oak Ridge earthflow

Time (Yr)	Pressure Perturbation (Pa)	τ (Pa)	σ (Pa)	Velocity (m/yr)	$V_{\circ}$ (m/yr)
1982.7105	18439.6	33998	126880	0.033841939	0.365
1983.0271	27477.1	33998	126880	0.055933208	
1983.0937	28631	33998	126880	0.43773846	
1983.2108	28467.6	33998	126880	0.46744216	
1983.2427	26538.1	33998	126880	0.54421538	
1983.3092	28214.1	33998	126880	0.64263732	
1983.3678	24817.1	33998	126880	0.19805871	
1983.4716	23982.6	33998	126880	0.02581534	
1983.7829	22268.2	33998	126880	0.24106442	
1983.8494	26504.4	33998	126880	1.0373075	
1983.8707	27090.8	33998	126880	1.5661309	
1983.9452	26749.3	33998	126880	1.1720937	
1984.049	27026.6	33998	126880	0.80543877	
1984.0783	28776.7	33998	126880	0.89493192	
1984.0969	28552.6	33998	126880	1.5489207	
1984.1129	28189.1	33998	126880	1.4382835	
1984.1342	27996.1	33998	126880	1.118665	

1984.1608	28676.3	33998	126880	2.8976151	
1984.2433	28491.8	33998	126880	2.7742891	
1984.2805	28231.1	33998	126880	2.9532755	
1984.3231	28002.1	33998	126880	2.6631443	
1984.363	26226.4	33998	126880	2.0941408	
1984.3897	26313.1	33998	126880	1.929697	
1984.4269	25849.3	33998	126880	0.12429611	
1984.8208	26292	33998	126880	0.13615068	
1985.1747	27229.5	33998	126880	0.33995791	
1985.2306	26741.6	33998	126880	0.57531338	
1985.3051	25772.4	33998	126880	0.082427951	
1985.6856	20322	33998	126880	0.042243297	

Table S3. Pore pressure and displacement data for Minor Creek earthflow